ACS APPLIED MATERIALS & INTERFACES

www.acsami.org

Research Article

Nanostructure- and Orientation-Controlled Resistive Memory Behaviors of Carbohydrate-*block*-Polystyrene with Different Molecular Weights via Solvent Annealing

Tsung-Han Chuang, Yun-Chi Chiang, Hui-Ching Hsieh, Takuya Isono, Chao-Wei Huang, Redouane Borsali, Toshifumi Satoh,* and Wen-Chang Chen*

Cite This: *ACS Appl. Mater. Interfaces* 2020, 12, 23217−23224

Read Online

ACCESS | Metrics & More | Article Recommendations | Supporting Information

ABSTRACT: We report the resistive electrical memory characteristics controlled by the self-assembled nanostructures of maltoheptaose-*block*-polystyrene (MH-*b*-PS) block copolymers, where the MH and PS blocks provide the charge-trapping and the insulating tunneling layer, respectively. A simple solvent annealing process, with various annealing conditions, were introduced for MH-*b*-PS thin films to achieve disordered, orientated cylinders and ordered-packed spheres morphologies. More details about the self-assembled MH-*b*-PS nanostructures, coupled with different volume fractions between MH and PS blocks, were investigated using atomic force microscopy and grazing-incidence small-angle X-ray scattering analyses. Moreover, various electrical memory behaviors including nonvolatile write-once-read-many-times (WORM) and Flash, and volatile dynamic-random-access-memory (DRAM) could be obtained by the same material (MH-*b*-PS_{3k}). This study establishes a detailed relationship between the nanostructure of the MH-*b*-PS-based block copolymers and their memory behavior of the resistive memory devices.

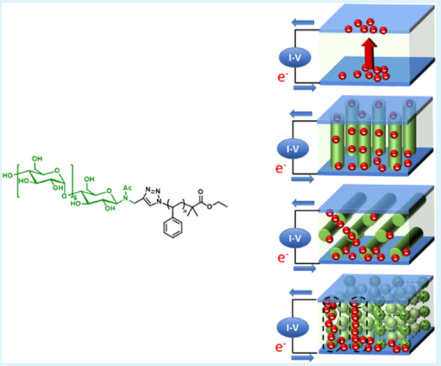

KEYWORDS: *block copolymer, maltoheptaose, nanostructure, solvent annealing, resistive memory*

1. INTRODUCTION

In the modern society of massive data storage, the development of resistive-type memories has attracted great research attention due to the simplified architecture of devices, lower power consumption, and fast switching ability.[1−4] Polymeric materials for the active layer of resistive memories have been recognized to be promising alternatives to their inorganic counterparts due to the advantage of facile solution-processability, low cost, flexibility, stretchability, and tailorable properties through molecular design.[5−12] In addition, versatile memory behaviors in the polymer-based resistive memory devices have been discovered including volatile and nonvolatile memories, such as dynamic-random-access-memory (DRAM), Flash and write-once-read-many-times memory (WORM). Such electrical behaviors can be controlled by donor/acceptor[13] characteristics of the polymer active layer or nanostructure[14−16] of the polymer-based active layer. The highly ordered-packed nanostructure might stabilize the charge-trapping and transport through the electrodes;[15] therefore, block copolymer (BCP) should be a suitable candidate for resistive memory active layer due to its capability of forming a packed nanoscale morphology.

A variety of BCPs, such as conjugated polymer-based BCPs,[17−19] ionic BCPs,[20,21] and carbohydrate-based BCPs,[11] have been developed so far for application in the polymer-based resistive memory devises. Among them, carbohydrate-based BCPs are particularly unique and interesting as the active layer because of the renewability of its raw materials. These kinds of green BCPs have reported to form highly ordered nanostructures with sub-10 nm domain spacing due to their high Flory−Huggins interaction parameter (χ) and small degree of polymerization (N).[22−25] Furthermore, the abundant hydroxyl group on the oligo- and polysaccharide, which is one of blocks in the BCPs, is known to exhibit a strong ability to trap electrons upon applying an external voltage.[11,26,27] These characteristics of carbohydrate-based BCPs represent a promising candidate for future advances in electronic memory devices. Indeed, our groups discovered the resistive memory behaviors in the carbohydrate-*block*-polyisoprene (MH-*b*-PI) block copolymer.[11]

To establish a blueprint for designing resistive memory materials, it is important to understand the relationship between the memory behavior and BCP nanostructure.

Received: March 10, 2020
Accepted: April 24, 2020
Published: April 24, 2020

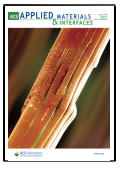

Downloaded via SYNCHROTRON RADIATION RESEARCH on January 27, 2021 at 03:18:50 (UTC).
See https://pubs.acs.org/sharingguidelines for options on how to legitimately share published articles.

© 2020 American Chemical Society

However, such information has been rarely reported. For example, Kim and co-workers have discussed the variety of morphologies makes BCPs (PS_m-*b*-$PCzMA_n$) exhibit different memory behaviors.[15] Our group also reported stretchable memory devices using carbohydrate-based BCP and discussed the relationship between the nanostructure and their corresponding memory behavior.[11] However, in both earlier studies, different nanostructures were achieved either by employing the BCPs with different volume fractions or by modifying the surface characteristics of the substrate. Such intrinsic differences may be a problem in the discussion about how the nanostructure actually affects memory behavior. To address this deficiency, the further post-treatment, such as thermal annealing and solvent annealing, to a BCP thin films should be a promising way to obtained different morphologies from one material.[28−34] Bosworth and co-workers reported that the choice of solvent for annealing allows for control of the self-assembled morphology of the BCPs.[28,29] Our group also reported a series of literatures about controlling the morphology of carbohydrate-based BCPs by various solvent vapor annealing conditions.[23,25] Furthermore, the solvent treatment is widely used in the fabrication of electronic devices, such as photovoltaics[35−38] and transistor devices,[39,40] to enhance their electrical performance in the recent years. Therefore, it would be interesting to use the solvent vapor annealing technique to control the nanostructure of the active layer thin film for the advanced resistive memory device, helping us to establish a more complete relationship between nanostructures and memory properties based on a favorable material.

In this study, we demonstrate a simple strategy for controlling the nanostructures of the carbohydrate-based BCP and the maltoheptaose-*block*-polystyrene (MH-*b*-PS) and report the memory behaviors of the sandwiched (indium tin oxide (ITO)/active layer/Al) resistive memory device depending on various post-treatments of MH-*b*-PS thin films as an active layer, as shown in Figure 1. We here selected three

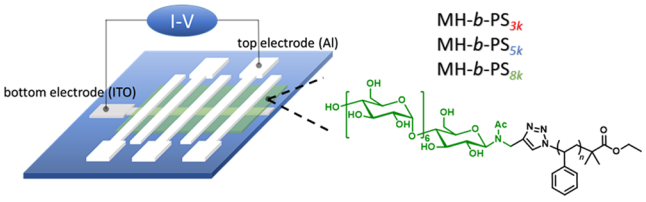

Figure 1. Schematic diagram of ITO/MH-*b*-PS_n/Al sandwiched structure based resistive memory device and the molecular structure of MH-*b*-PS_n (n = 3k, 5k, and 8k).

different block ratios of MH-*b*-PS_n for comprehensively understanding the nanostructure (Table 1). MH-*b*-PS consists of a hydrophilic MH block and a hydrophobic PS block, which serve as charge-storage sites and an insulating matrix, respectively. The thin films of MH-*b*-PS_n were annealed by tetrahydrofuran (THF)/H_2O mixed solvent or pure THF, accordingly to that H_2O is a good solvent for MH and a poor one for PS, while THF is a good solvent for PS and a poor one for MH. Therefore, THF or H_2O vapor can impart mobility to the BCP thin film, which is necessary to enable the rearrangement and enhancement of nanostructure ordering. The well-controlled nanostructures were identified using atomic force microscopy (AFM) and grazing-incidence small-angle X-ray scattering (GISAXS). Finally, we have demonstrated successfully controlling various nanostructures of MH-*b*-PS thin film using the same material, which revealed a clear relationship between the memory performance and the active layer nanostructure. In addition, the morphology and memory performance of MH-*b*-PS thin films with different volume block ratios were also discussed, which further deepen the carbohydrate-based BCP design for resistive memory device applications.

2. EXPERIMENTAL SECTION

2.1. Materials. According to our previous reports,[23,26] the BCPs, maltoheptaose-*block*-polystyrene (MH-*b*-PS_n), with $M_{n,PS}$ = 3000, 5000, and 8000 g mol^{-1}, were synthesized through copper-catalyzed azido-alkyne cycloaddition (CuAAC) of *N*-maltoheptaosyl-3-acetamido-1-propyne and azido-terminated polystyrene. THF (anhydrous) and methonol (anhydrous) were purchased from Sigma-Aldrich (Missouri). Glass substrates with ITO pattern was purchased from Luminescence Technology Corp (Taiwan).

2.2. Morphology Characterization. For solvent annealing treatment, thin films on a Petri dish were put in a tightly capped 2 L glass bottle containing an uncapped 20 mL beaker filled with a mixture of 2.5 g of THF and 2.5 g of water or a pure 5 g THF. The nanostructure of polymer films was visualized with a Nanoscope 3D controller AFM (Digital Instruments) operated in the tapping mode under ambient atmosphere. The spring constant of the silicon cantilevers (Nanosensor PPP-SEIHR) was 15 N m^{-1} and the resonant frequency was 330 kHz. GISAXS analysis of polymer thin films were conducted on beamline BL23A1 in the National Synchrotron Radiation Research Center (NSRRC), Taiwan.

2.3. Fabrication and Characterization of Resistive Memory Devices. The resistive memory devices were fabricated using the studied copolymers with an ITO/MH-*b*-PS thin film (60−70 nm)/Al sandwiched structure. Patterned ITO glasses were first precleaned by an ultrasonic cleaning process in deionized water, isopropanol, and acetone successively for 10 min. On the other hand, the polymer solution in the concentration of 10 mg mL^{-1} were prepared in mixing solvent (THF/methanol = 9/1 (v/v)) and filtered through a polytetrafluoroethylene filter membrane with a 220 nm pore size. Thin films of 60−70 nm were deposited onto the ITO glasses via spin-coating at a speed rate of 3000 rpm for 60 s, where the thickness of these active layers was further checked by surface profilometer. In addition, a solvent annealing process (under the mixture of THF/H_2O = 10/1 (w/w) or pure THF) was introduced to adjust the nanostructure within polymer thin films and cause differences in their electrical characterizations of resistive memory device simply through controlling the process time. Finally, 45 nm Al top electrodes were deposited using a thermal evaporator under a pressure of 10^{-7} Torr. The top electrodes were aligned by a shadow mask, which is perpendicular to the bottom ITO electrodes, leading to cross-point arrays of memory cells with active joint areas of 0.2 × 0.2, 0.4 × 0.4, and 0.6 × 0.6 mm^2, respectively. All of the measurements of fabricated devices were conducted using a Keithley 4200-SCS semiconductor parameter analyzer (Keithley Instruments Inc., Cleveland, OH), with a Remote PreAmp (4200-PA) in a N_2-filled glovebox. Triaxial cables were connected into the probe station to minimize the background noise.

3. RESULT AND DISCUSSION

3.1. Morphology of MH-*b*-PS_n Thin films. Thin films of studied BCPs, with a thickness of 60−70 nm, were prepared on a Si wafer by spin-coating from a mixture of THF and methanol, where THF is a good solvent for PS block and methanol dissolves MH block well. After that, pure THF or mixture of THF/H_2O = 10/1 (w/w) was chosen as the annealing solvent for tuning thin-film morphologies. The surface structure of the cast MH-*b*-PS thin films were visualized by AFM, as shown in Figure 2. For the case of the

https://dx.doi.org/10.1021/acsami.0c04551
ACS Appl. Mater. Interfaces 2020, 12, 23217−23224

Table 1. Solvent Annealing Conditions and the Resulting Morphologies of MH-*b*-PS$_n$ Thin Films

nomenclature	material	f_{MH}	annealing solvent (w/w)	time (h)	nanostructure
MHPS$_{3k}$	MH-*b*-PS$_{3k}$	0.29		0	disorder
MHPS$_{3k}$-5h			THF/H$_2$O = 10/1	5	vert. cylinder
MHPS$_{3k}$-24h			THF/H$_2$O = 10/1	24	horiz. cylinder
MHPS$_{3k}$-THF			THF/H$_2$O = 1/0	22	order packed sphere
MHPS$_{5k}$	MH-*b*-PS$_{5k}$	0.17		0	disorder
MHPS$_{5k}$-5h			THF/H$_2$O = 10/1	5	disorder
MHPS$_{5k}$-24h			THF/H$_2$O = 10/1	24	horiz. cylinder/sphere
MHPS$_{5k}$-THF			THF/H$_2$O = 1/0	22	disorder
MHPS$_{8k}$	MH-*b*-PS$_{8k}$	0.12		0	disorder
MHPS$_{8k}$-5h			THF/H$_2$O = 10/1	5	disorder
MHPS$_{8k}$-24h			THF/H$_2$O = 10/1	24	disorder
MHPS$_{8k}$-THF			THF/H$_2$O = 1/0	22	disorder

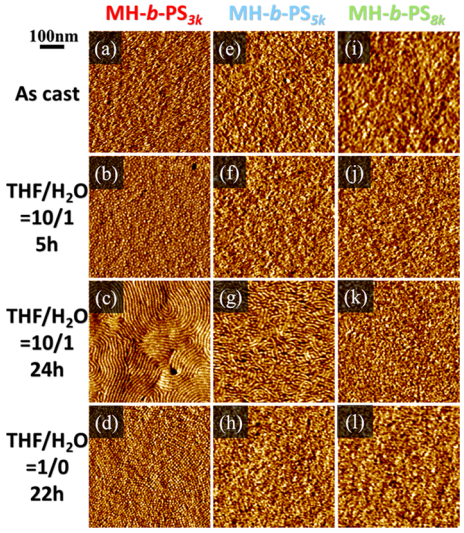

Figure 2. Tapping mode AFM phase images of the MH-*b*-PS$_n$ thin films with different postannealing treatments.

as-cast thin films, MH-*b*-PS$_{3k}$ (MHPS$_{3k}$), MH-*b*-PS$_{5k}$ (MHPS$_{5k}$), and MH-*b*-PS$_{8k}$ (MHPS$_{8k}$) showed featureless surfaces. However, MHPS$_{3k}$ turned into packed dots and a fingerprint-like surface as the annealing process time increased to 5 h (MHPS$_{3k}$-5h) and 24 h (MHPS$_{3k}$-24h) under mixed-solvent annealing environment. Similar ordered-packed dots could be obtained if MHPS$_{3k}$ was annealed in pure THF for 22 h (MHPS$_{3k}$-THF). This postannealing process was also carried out for MHPS$_{5k}$ and MHPS$_{8k}$ thin films at the same time; however, only a mixed structure of dots and fingerprint-like structure could be observed when MHPS$_{5k}$ films were annealed in the mixture for 24 h (MHPS$_{5k}$-24h). No specific morphology was found in those two BCPs in other annealing conditions. That is, in the case of MHPS$_{5k}$ and MHPS$_{8k}$ thin films except MHPS$_{5k}$-24h, only disorder nanostructure was observed regardless of the annealing condition. The above-mentioned results indicate that the nanostructures of the studied BCPs can be tuned by both solvent annealing conditions (process times and different solvents) and varying volume fractions between the two blocks.

To gain more insight into the nanostructure and micro-domain orientation in the studied BCP thin films, same samples were also subjected to the GISAXS experiment. The two-dimensional (2D) GISAXS patterns and the corresponding one-dimensional (1D) profiles along with the q_y direction of four circumstances are shown in Figure 3. As shown in

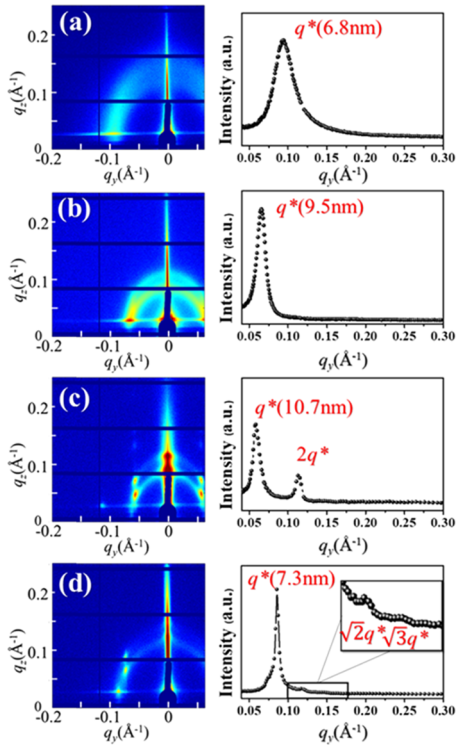

Figure 3. 2D-GISAXS patterns and the corresponding q_y scans of the MH-*b*-PS$_{3k}$ thin films. (a) MHPS$_{3k}$, (b) MHPS$_{3k}$-5h, (c) MHPS$_{3k}$-24h, and (d) MHPS$_{3k}$-THF.

Figure 3a, MHPS$_{3k}$ thin film exhibits a vague ringlike pattern, indicating that MH domains are randomly oriented. This coincided with the fact that the AFM image (Figure 2a) showed disordered structure. The domain spacing was determined to be 6.8 nm by the relation $d = 2\pi/q^*$ from 1D profiles of q_y scan. 2D-GISAXS pattern and AFM image of MHPS$_{3k}$-5h thin film (Figures 3b and 2b) together suggest that the cylindrical MH domains are oriented vertically to the substrate with the domain spacing of 9.5 nm. This result is similar to our previous literatures.[26] The dots in the AFM images of Figure 2b may represent the cross section of vertical cylinder structures. After annealing for a longer time, the nanostructure becomes more ordered and oriented; therefore, higher-ordered scattering peaks appear in the 2D-GISAXS pattern and the corresponding q_y scans in Figure 3c,d. In Figure 3c, the higher-ordered peaks can be seen both in the q_y and q_z directions. By combining with the AFM results (Figure

https://dx.doi.org/10.1021/acsami.0c04551
ACS Appl. Mater. Interfaces 2020, 12, 23217−23224

2c), the morphology of MHPS$_{3k}$-24h thin films can be assigned to be horizontal cylinder structures, which is well parallel to the substrate with the domain spacing of 10.7 nm. The 2D-GISAXS image shows the typical scattering pattern of the body-centered cubic (BCC) sphere structure, and higher-order peaks scatter from q_y equals $1:\sqrt{2}:\sqrt{3}$ in Figure 3d. Therefore, we conclude that the MHPS$_{3k}$-THF thin film has a BCC sphere structure. Table 1 summarizes the results of the nanostructure of the studied BCP thin films. These results reveal that a variety of nanostructures involving the disordered, vertical cylinder, horizontal cylinder, and BCC sphere nanostructures can be obtained from single BCP thin films (MHPS$_{3k}$) simply through optimizing the solvent annealing condition carefully.

In the mixture solvent annealing system, the reason for the transformation of nanostructure is the disparity in polarity between the MH and the PS segments, as well as the vapor composition during the annealing process. MH possesses abundant hydroxyl groups that show high hydrophilicity and high solubility in water; in contrast, PS is hydrophobic and more soluble with organic solvents, such as THF. During annealing, the processing solvent mixture can swell MH and PS blocks at the same time, promoting the motion of each BCP molecule to a more thermodynamically stable cylinder structure. The orientation of the cylinder structure should be related to the volatility between THF and water. Since THF is more volatile than water, the vapor inside the well-sealed closed system has a higher THF content in the early stage, and thus forcing the MH domain to exhibit an orientation that is less contact with plenty of THF vapor, forming the vertical cylinderal structure between interfaces with atmosphere and substrate. As the time progresses, the vapor content of H_2O will lately increase and achieve an equilibrium, allowing the MH domains emerge to the surface and therefore form a more thermodynamically favorable horizontal cylinderal structure. Moreover, when it comes to using pure THF as the annealing solvent, only the PS domains can be swollen, decreasing the volume fraction of the MH blocks (f_{MH}) and cause the horizontal shift in the equilibrium position in the phase diagram of BCP, leading to an order−order transition from a cylinderal to a spherical morphology. These morphologies can be maintained upon rapid drying after solvent annealing.

Figure 2e−h shows the AFM images of the MH-*b*-PS$_{5k}$ thin films under identical annealing conditions. The thin film without annealing (MHPS$_{5k}$) and with annealing for 5 h in the mixed solvent (MHPS$_{5k}$-5h) show a disordered structure in their AFM images. Interestingly, thin films annealed for 24 h in a mixed solvent (MHPS$_{5k}$-24h) shows a cylinderal/spherical mixed nanostructure. Because of the decrease in f_{MH}, the equilibrium position in the BCP phase diagram is located close on the boundary between regions of cylinder and sphere. However, in the pure THF annealing system (MHPS$_{5k}$-THF), the AFM image (Figure 2h) shows a disordered structure again. The reason is similar to the case of MH-*b*-PS$_{3k}$; the swelling effect of the PS blocks only makes a more severe difference between the volume faction of MH and PS, thus causing the shift in the equilibrium position of morphology from the cylinderal/spherical mixed structure to the disorder area. Figure 2i−l shows the AFM images of the as-cast and annealed thin films of MH-*b*-PS$_{8k}$. All of the images seem to have a disordered structure. This is attributed to the low volume fraction of the MH block (fMH = 0.12), resulting in the morphology of MH-b-PS8k thin films locate on the disorder region in thermodynamic equilibrium. More GISAXS results of thin films on MHPS$_{5k}$ and MHPS$_{8k}$ with various postannealing treatment are shown in Figure S1 and S2 (SI).

Overall, we successfully demonstrated how to easily control the thin-film morphologies of MH-*b*-PS$_n$ BCPs either by their intrinsic properties (i.e., volume fraction of MH) or via the post-treatment process (i.e., solvent annealing). The above-mentioned nanostructures as well as the corresponding domain spacing are both important factors that change the electrical behaviors of resistive-type memory devices in the following sections.

3.2. Electrical Characterization of MH-*b*-PS$_n$-Based Resistive Memory Devices. The architecture of the studied resistive memory devices is shown in Figure 1, a sandwiched structure of indium tin oxide (ITO), MH-*b*-PS$_n$ thin films (60−70 nm), and top aluminum (Al) electrode. Morphologies of the BCP thin films on ITO were also checked by AFM (Figure S3, SI) and GISAXS (Figure S4, SI). The results are similar to those on the silicon substrate under the same solvent annealing conditions, indicating that the difference in ITO and Si wafer does not affect morphology significantly. The GISAXS data of MHPS$_{3k}$-5h thin films with different thicknesses are also analyzed in Figure S5 (SI). Based on these results, the optimal film thickness for fabricating devices is around 60−70 nm. The manipulation procedure is detailed as follows: as the Al top electrode was grounded, the applied voltage bias, with a step of 0.05 V, is passed through the bottom ITO electrode. This applied power was set to turn off immediately after each programming process. The representative current−voltage (I−V) characteristics of the devices are shown in Figure 4. Note that the results data are averaged from 18 devices in three different batches, and the overall performance are summarized in Table 2.

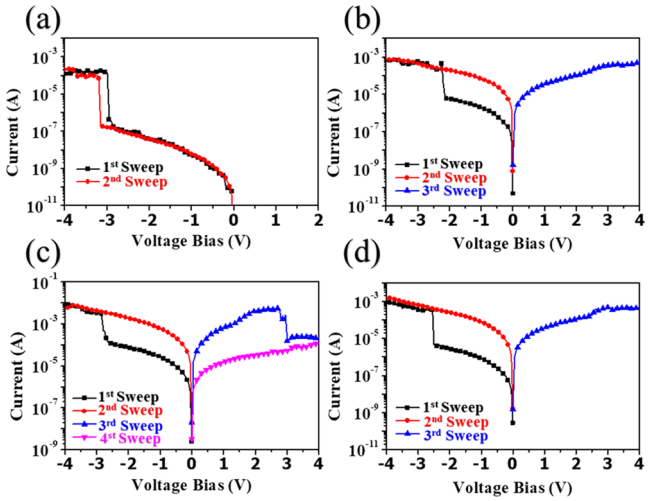

Figure 4. I−V characteristics of the MH-*b*-PS$_{3k}$ as-cast and solvent-annealed thin films for resistive memory devices. (a) MHPS$_{3k}$, (b) MHPS$_{3k}$-5h, (c) MHPS$_{3k}$-24h, and (d) MHPS$_{3k}$-THF.

In Figure 4a, the resistive memory device with MHPS$_{3k}$ as the active layer was initially in a high-resistance state (HRS), or an OFF state, during the first sweep from 0 to −3.10 V; suddenly, the current underwent a distinctive steplike increase at −3.10 V (V_{set}), turning into a low-resistance state (LRS), or an ON state. This electrical transition from the HRS to the LRS is defined as the "SET" or "writing" process.

https://dx.doi.org/10.1021/acsami.0c04551
ACS Appl. Mater. Interfaces 2020, 12, 23217−23224

Table 2. Electrical Characteristic of MH-*b*-PS$_n$-Based Resistive Memory Devices

nomenclature	memory behavior	V_{set}[a] (V)	I_{on}/I_{off}[a]
MHPS$_{3k}$	DRAM	−3.10 ± 0.23	~10^3
MHPS$_{3k}$-5h	WORM	−2.20 ± 0.12	~10^2
MHPS$_{3k}$-24h	Flash	−2.85 ± 0.26	~10^1
MHPS$_{3k}$-THF	WORM	−2.50 ± 0.21	~10^2
MHPS$_{5k}$	DRAM	−3.20 ± 0.12	~10^2
MHPS$_{5k}$-5h	DRAM	−2.90 ± 0.31	~10^3
MHPS$_{5k}$-24h	WORM	−2.25 ± 0.21	~10^2
MHPS$_{5k}$-THF	DRAM	−3.15 ± 0.15	~10^3
MHPS$_{8k}$	DRAM	−3.60 ± 0.17	~10^2
MHPS$_{8k}$-5h	DRAM	−2.95 ± 0.24	~10^2
MHPS$_{8k}$-24h	DRAM	−3.25 ± 0.11	~10^2
MHPS$_{8k}$-THF	DRAM	−3.05 ± 0.19	~10^2

[a]Average from 18 devices of 3 different batches.

Subsequently, the second sweep was utilized after few seconds, and the device went back to its original HRS (OFF state) at low voltage (<3 V) and again turned into LRS when the applied voltage was around −3.20 V, resembling the *I*−*V* characteristic of the first sweep. This type of *I*−*V* behavior, reversely turning back to HRS (OFF state) when the electric power is immediately turn off, is typically categorized as volatile DRAMs. Figure 4b shows another *I*−*V* characteristic of the device using MHPS$_{3k}$-5h as the active layer. When a negative bias was applied (first sweep), the current was initially low (HRS, OFF state) and abruptly increased to high current (LRS, ON state) at −2.20 V (V_{set}). This device remained in the LRS (ON state) during the period of the following sweeps, both in the negative direction (second sweep) and the positive direction (third sweep). Therefore, the device with MHPS$_{3k}$-5h, which remains in the LRS after turning off the electric power or even applying a reverse bias, exhibits a nonvolatile WORM (write-once-read-many) characteristic. Moreover, the long-term stability of the device with ON state can be maintained for at least 10^4 s at a reading bias of −1.0 V (Figure 5a). A totally different *I*−*V* characteristic for the device using MHPS$_{3k}$-24h as the active layer was obtained as shown in Figure 4c. Initially, the device was in its HRS (OFF state), and the current then shifted to LRS (ON state) at −2.85 V (V_{set}) as the applied voltages increased during the first sweep. The LRS (ON state) can be maintained after the applied power was turned off and also during the second sweep (second sweep). Subsequently, when a positive sweep (third sweep) was applied, the device moved back to its original HRS (OFF state) with a current dropping at approximately 2.60 V. This sweeping curve is defined as the "erasing" process. Further sweeping with a positive bias (fourth sweep) does not change the state of the device. Such a memory behavior, turning off using a reverse bias, is defined as a nonvolatile Flash-type memory. In addition, the long-term stability of this Flash-type device can also remain at least 10^4 s both with the ON and OFF states when the reading bias was set at −1.0 V (Figure 5b). Moreover, the reversible stability of the device was further tested by repeated writing/reading/erasing/reading (WRER) operation (Figure S6, SI), which revealed sufficient stability at least up to 50 cycles. When using the MHPS$_{3k}$-THF active layer, as shown in Figure 4d, the *I*−*V* characteristic of the device is similar to the one with MHPS$_{3k}$-5h, while having a larger V_{set} = −2.50 V. The device is also categorized as a

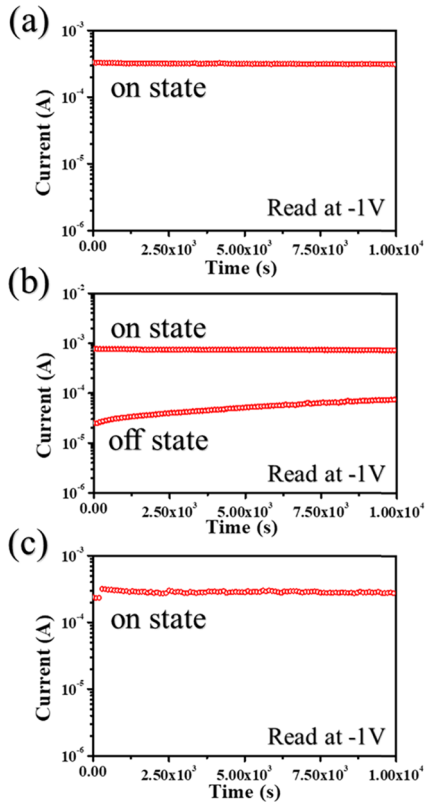

Figure 5. Memory retention characteristics of the MH-*b*-PS$_{3k}$ based resistive memory devices. (a) MHPS$_{3k}$-5h, (b) MHPS$_{3k}$-24h and (C) MHPS$_{3k}$-THF.

WORM-type memory, and the corresponding retention ability is shown in Figure 5c.

It is apparent that the thin-film nanostructure has a significant influence on memory behavior. If the thin film has a disordered nanostructure, the device exhibits a volatile DRAM memory behavior. When it comes to a vertical cylinder or ordered-packed sphere nanostructures, the devices possess a nonvolatile WORM memory behavior, and as horizontal cylindrical nanostructure was established, the device reveals a nonvolatile flash memory behavior. These results indicate that the desired memory behavior can be realized by simply tuning the active layer nanostructure of the same material.

Device behaviors based on MH-*b*-PS$_{5k}$ and MH-*b*-PS$_{8k}$ were further investigated. As mentioned before, those two BCPs mainly form disordered structures because of the highly asymmetric compositions. As expected from the results of MH-*b*-PS$_{3k}$, the devices with a disordered thin-film morphology (MHPS$_{5k}$, MHPS$_{5k}$-5h, MHPS$_{5k}$-THF, MHPS$_{8k}$, MHPS$_{8k}$-5h, MHPS$_{8k}$-24h, and MHPS$_{8k}$-THF) exhibit a DRAM memory behavior (see Figure S7 and S8, SI for their *I*−*V* characteristics). Thus, the relationship between morphology and memory behavior is consistent despite using different volume fractions of BCPs. Interestingly, a nonvolatile WROM-type memory behavior was observed with MHPS$_{5k}$-24h. It is thought to be due to the mixed horizontal cylindrical/spherical morphology. Nevertheless, the above results revealed a clear relationship between the BCP nanostructure and the memory behavior of resistive memory devices.

In addition to memory behavior, another noteworthy thing is that the V_{set} also demonstrated some relation to the resulted morphologies. As summarized in Table 2, the DRAM memory

https://dx.doi.org/10.1021/acsami.0c04551
ACS Appl. Mater. Interfaces 2020, 12, 23217−23224

behavior of $MHPS_{3k}$ possessed the largest V_{set} (−3.10 V) since there are less number of trapping sites for electrons to transport within the active polymer thin film. The $MHPS_{3k}$-24h device (Flash) has the second-largest V_{set} (−2.85 V), which may be attributed to the discontinuous morphology and large domain spacing (10.7 nm) when electrons crossed two electrodes. Further, the case of $MHPS_{3k}$-THF shows a third V_{set} of −2.50 V, which resulted from the smaller domain spacing (7.3 nm). And last, for the device of MHPS3k-5h with WORM-type memory, continuous vertical cylinders offer a direct transporting channel and thus causing the smallest Vset (-2.20V). Interestingly, V_{set} demonstrated an upward trend when the volume fraction of the PS block increased, which could be seen from the results of $MHPS_{3k}$ (V_{set} = −3.10 V), $MHPS_{5k}$ (V_{set} = −3.20 V), and $MHPS_{8k}$ (V_{set} = −3.60 V). The above-mentioned results indicate that morphology, domain spacing, and volume fraction of the MH domain have an impact on the resulted V_{set}.

3.3. Proposed Mechanism for MH-*b*-PS_n-Based Memory Behavior. According to our results, the plentiful hydroxyl groups in the MH moieties of the MH-*b*-PS_n have the ability to trap electrons by undergoing an electrochemical reaction via external electric fields. The electrons initially accumulated on the PS/MH interfaces and formed an active pathway for charge transportation between two electrodes when a large enough electrical field was applied, thus altering the resistance states within the BCP active layer. On the other hand, the PS blocks provided an insulting matrix that forms different morphologies with MH blocks and led to different electrical behaviors of memory devices.

In the studied MH-*b*-PS_n-based devices, multiple memory types, such as DRAM, WORM, and Flash, could be achieved by tuning the nanostructures between disordered, vertical cylinder, horizontal cylinder, and ordered-packed sphere. The orientations, domain spacings, and nanostructures of the MH microdomain, which serves as an electron-trapping site, are the key factors that dominate memory behavior. As proposed in Figure 6a, the disordered structure does not provide a stable trapping site for electrons because of the discontinuity and irregularity; therefore, the LRS will be lost when removing the external voltage bias, leading to a DRAM memory behavior. On the other hand, when the MH domains form cylindrical structures perpendicular to both electrodes, a continuous active pathway can be created for the electron transfer, which leads to a WROM memory behavior with a relatively smaller V_{set} (Figure 6b). However, the horizontal cylinder is only continuous in the lateral orientation, providing stable trapping sites for electrons, but dissociates in the direction perpendicular to the electrodes (Figure 6c). Because the MH cylinder is separated by the PS insulting matrix, the trapped charges can be erased via reverse bias, leading to a flash-type memory behavior. Also, in the last case of the ordered-packed sphere morphology (BCC), although it is discontinuous in both lateral and perpendicular directions, the smaller inter-sphere distance (5.1 nm, Figure S9, SI) in the vertical direction allows electrons to be transferred easily, forming an active pathway similar to that in the case of a vertical cylindrical structure (Figure 6d) and resulting in a WORM-type memory behavior, with a relatively higher V_{set} (−2.50 V) compared to that of the vertical cylinder (−2.20 V). Meanwhile, the $MHPS_{5k}$-24h thin film, with the morphology of a mixed cylindrical/spherical structure, demonstrates a WORM-type memory behavior owing to the easier penetrated pathways that dominated the spherical morphology. To sum up, the controllable BCP nanostructures were successfully established via simple solvent annealing and their morphology-related memory behaviors including DRAM, WORM, and Flash were also systematically revealed.

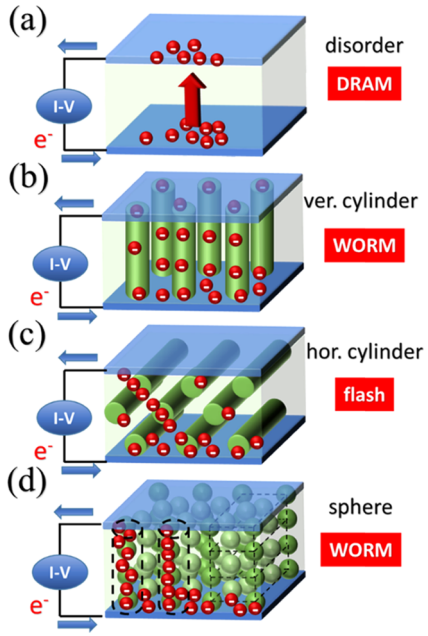

Figure 6. Proposed mechanism for charge transportation within the MH-*b*-PS_{3k} active layer of the studied resistive memory devices.

4. CONCLUSIONS

In this study, we systematically analyze the nanostructure of MH-*b*-PS_n thin films under various solvent annealing conditions. A proposed mechanism of the relationship between the nanostructures and their related electrical memory behavior was established. Through the precise control of the thin-film morphology, we also successfully demonstrated that the orientations, domain spacings, and continuity of the nanostructures of MH microdomains are critical key factors that determine the properties of memory performance (memory type and setting voltages, V_{set}). More specifically, diverse nanostructures could be obtained, including disordered, vertical cylinder, horizontal cylinder, and ordered-packed sphere by a favorable material (MH-*b*-PS_{3k}) by extending the annealing time or adjusting the solvent ratio of the annealing solvent. Thus, we open up the route that several typical types of memory could be achieved using only one material and give great importance to the future design of the next-generation electronics.

■ ASSOCIATED CONTENT

Supporting Information

The Supporting Information is available free of charge at https://pubs.acs.org/doi/10.1021/acsami.0c04551.

More analyses on 2D-GISAXS patterns; corresponding 1D profiles; tapping mode AFM phase images; *I*−*V* curves; and endurance cycling test of fabricated devices (PDF)

https://dx.doi.org/10.1021/acsami.0c04551
ACS Appl. Mater. Interfaces 2020, 12, 23217−23224

AUTHOR INFORMATION

Corresponding Authors

Toshifumi Satoh − *Faculty of Engineering, Hokkaido University, Sapporo 060-8628, Japan;* orcid.org/0000-0001-5449-9642; Email: satoh@eng.hokudai.ac.jp

Wen-Chang Chen − *Department of Chemical Engineering and Advanced Research Center for Green Materials Science and Technology, National Taiwan University, Taipei 10617, Taiwan;* orcid.org/0000-0003-3170-7220; Email: chenwc@ntu.edu.tw

Authors

Tsung-Han Chuang − *Department of Chemical Engineering, National Taiwan University, Taipei 10617, Taiwan*

Yun-Chi Chiang − *Department of Chemical Engineering, National Taiwan University, Taipei 10617, Taiwan*

Hui-Ching Hsieh − *Department of Chemical Engineering, National Taiwan University, Taipei 10617, Taiwan*

Takuya Isono − *Faculty of Engineering, Hokkaido University, Sapporo 060-8628, Japan;* orcid.org/0000-0003-3746-2084

Chao-Wei Huang − *Department of Chemical Engineering, National Taiwan University, Taipei 10617, Taiwan*

Redouane Borsali − *Univ. Grenoble Alpes, CNRS, CERMAV, F-38000 Grenoble, France*

Complete contact information is available at: https://pubs.acs.org/10.1021/acsami.0c04551

Notes

The authors declare no competing financial interest.

ACKNOWLEDGMENTS

The authors appreciate the financial supports by "Advanced Research Center for Green Materials Science and Technology" from the Featured Area Research Center Program within the framework of the Higher Education Sprout Project by the Ministry of Education (108L9006), the Ministry of Science and Technology in Taiwan (MOST 108-3017-F-002-002), the JSPS KAKENHI (19H02769), the Frontier Chemistry Center (in Hokkaido University), and the Photo-excitonix Project (in Hokkaido University). The authors also acknowledge the National Synchrotron Radiation Research Center of Taiwan for facilitating the GISAXS (BL23A) experiments. The technical assistance and helpful discussion with Chien-Chung Shih and Chih-Chien Hung are also appreciated. T.I. gratefully acknowledges the Nanotech CUPAL NRP program.

REFERENCES

(1) Cho, B.; Song, S.; Ji, Y.; Kim, T. W.; Lee, T. Organic Resistive Memory Devices: Performance Enhancement, Integration, and Advanced Architectures. *Adv. Funct. Mater.* **2011**, *21*, 2806−2829.

(2) Valov, I.; Linn, E.; Tappertzhofen, S.; Schmelzer, S.; van den Hurk, J.; Lentz, F.; Waser, R. Nanobatteries in Redox-Based Resistive Switches Require Extension of Memristor Theory. *Nat. Commun.* **2013**, *4*, No. 1771.

(3) Tappertzhofen, S.; Valov, I.; Tsuruoka, T.; Hasegawa, T.; Waser, R.; Aono, M. Generic Relevance of Counter Charges for Cation-Based Nanoscale Resistive Switching Memories. *ACS Nano* **2013**, *7*, 6396−6402.

(4) Lin, W. P.; Liu, S. J.; Gong, T.; Zhao, Q.; Huang, W. Polymer-Based Resistive Memory Materials and Devices. *Adv. Mater.* **2014**, *26*, 570−606.

(5) Liu, G.; Zhuang, X.; Chen, Y.; Zhang, B.; Zhu, J.; Zhu, C. X.; Neoh, K. G.; Kang, E. T. Bistable Electrical Switching and Electronic Memory Effect in a Solution Processable Graphene Oxide-Donor Polymer Complex. *Appl. Phys. Lett.* **2009**, *95*, No. 253301.

(6) Bhansali, U. S.; Khan, M. A.; Cha, D.; AlMadhoun, M. N.; Li, R.; Chen, L.; Amassian, A.; Odeh, I. N.; Alshareef, H. N. Metal-Free, Single-Polymer Device Exhibits Resistive Memory Effect. *ACS Nano* **2013**, *7*, 10518−10524.

(7) Hosseini, N. R.; Lee, J. S. Resistive Switching Memory Based on Bioinspired Natural Solid Polymer Electrolytes. *ACS Nano* **2015**, *9*, 419−426.

(8) Han, S. T.; Zhou, Y.; Roy, V. A. L. Towards the Development of Flexible Non-Volatile Memories. *Adv. Mater.* **2013**, *25*, 5425.

(9) Hsu, L. C.; Shih, C. C.; Hsieh, H. H.; Chiang, Y. C.; Wu, P. H.; Chueh, C. C.; Chen, W. C. Intrinsically Stretchable, Solution-Processable Functional Poly(siloxane-imide)s for Stretchable Resistive Memory Applications. *Polym. Chem.* **2018**, *9*, 5145.

(10) Chiang, Y. C.; Shih, C. C.; Tung, S. H.; Chen, W. C. Blends of Polythiophene Nanowire/Fluorine Rubber with Multiscale Phase Separation Suitable for Stretchable Semiconductors. *Polymer* **2018**, *155*, 146−151.

(11) Hung, C. C.; Chiu, Y. C.; Wu, H. C.; Lu, C.; Bouilhac, C.; Otsuka, I.; Halila, S.; Borsali, R.; Tung, S. H.; Chen, W. C. Conception of Stretchable Resistive Memory Devices Based on Nanostructure-Controlled Carbohydrate-block-Polyisoprene Block Copolymers. *Adv. Funct. Mater.* **2017**, *27*, No. 1606161.

(12) Chiang, Y. C.; Wu, H. C.; Wen, H. F.; Hung, C. C.; Hong, C. W.; Kuo, C. C.; Higashihara, T.; Chen, W. C. Tailoring Carbosilane Side Chains toward Intrinsically Stretchable Semiconducting Polymers. *Macromolecules* **2019**, *52*, 4396−4404.

(13) Yu, A. D.; Kurosawa, T.; Chou, Y. H.; Aoyagi, K.; Shoji, Y.; Higashihara, T.; Ueda, M.; Liu, C. L.; Chen, W. C. Tunable Electrical Memory Characteristics Using Polyimide:Polycyclic Aromatic Compound Blends on Flexible Substrates. *ACS Appl. Mater. Interfaces* **2013**, *5*, 4921−4929.

(14) Chen, J. C.; Liu, C. L.; Sun, Y. S.; Tung, S. H.; Chen, W. C. Tunable Electrical Memory Characteristics by the Morphology of Self-Assembled Block Copolymers:PCBM Nanocomposite Films. *Soft Matter* **2012**, *8*, 526.

(15) Kim, K.; Kim, Y. Y.; Park, S.; Ko, Y. G.; Rho, Y.; Kwon, W.; Shin, W. J.; Ree, M.; et al. Nanostructure- and Orientation-Controlled Digital Memory Behaviors of Linear-Brush Diblock Copolymers in Nanoscale Thin Films. *Macromolecules* **2014**, *47*, 4397−4407.

(16) Jung, S.; Kwon, W.; Wi, D.; Kim, J.; Ree, B. J.; Kim, Y. Y.; Kim, W. J.; Ree, M. Hierarchical Self-Assembly and Digital Memory Characteristics of Crystalline−Amorphous Brush Diblock Copolymers Bearing Electroactive Moieties. *Macromolecules* **2016**, *49*, 1369−1382.

(17) Verbakel, F.; Meskers, S. C. J.; Janssen, R. A. J. Electronic Memory Effects in a Sexithiophene-Poly(ethylene oxide) Block Copolymer Doped with NaCl. Combined Diode and Resistive Switching Behavior. *Chem. Mater.* **2006**, *18*, 2707−2712.

(18) Lian, S. L.; Liu, C. L.; Chen, W. C. Conjugated Fluorene Based Rod-Coil Block Copolymers and Their PCBM Composites for Resistive Memory Switching Devices. *ACS Appl. Mater. Interfaces* **2011**, *3*, 4504−4511.

(19) Arunagirinathan, R. N.; Gopikrishna, P.; Das, D.; Iyer, P. K. Solution Processed Donor−Acceptor Polymer Based Electrical Memory Device with High On/Off Ratio and Tunable Properties. *ACS Appl. Electron. Mater.* **2019**, *1*, 600−607.

(20) Suga, T.; Sakata, M.; Aoki, K.; Nishide, H. Synthesis of Pendant Radical- and Ion-Containing Block Copolymers via Ring-Opening Metathesis Polymerization for Organic Resistive Memory. *ACS Macro Lett.* **2014**, *3*, 703−707.

(21) Suga, T.; Aoki, K.; Yashiro, T.; Nishide, H. "Click" Incorporation of Radical/Ionic Sites into a Reactive Block Copolymer: A Facile and On-Demand Domain Functionalization Approach toward Organic Resistive Memory. *Macromol. Rapid Commun.* **2016**, *37*, 53−59.

(22) Otsuka, I.; Isono, T.; Rochas, C.; Halila, S.; Fort, S.; Satoh, T.; Kakuchi, T.; Borsali, R. 10 nm Scale Cylinder−Cubic Phase

Transition Induced by Caramelization in Sugar-Based Block Copolymers. *ACS Macro Lett.* **2012**, *1*, 1379−1382.
(23) Otsuka, I.; Tallegas, S.; Sakai, Y.; Rochas, C.; Halila, S.; Fort, S.; Bsiesy, A.; Baron, T.; Borsali, R. Control of 10 nm Scale Cylinder Orientation in Self-Organized Sugar-Based Block Copolymer Thin Films. *Nanoscale* **2013**, *5*, 2637.
(24) Isono, T.; Ree, B. J.; Tajima, K.; Borasli, R.; Satoh, T. Highly Ordered Cylinder Morphologies with 10 nm Scale Periodicity in Biomass-Based Block Copolymers. *Macromolecules* **2018**, *51*, 428−437.
(25) Liao, Y.; Goujon, L. J.; Reynaud, E.; Halila, S.; Gibaud, A.; Weia, B.; Borsali, R. Self-Assembly of Copper-Free Maltoheptaose-Block-Polystyrene Nanostructured Thin Films in Real and Reciprocal Space. *Carbohydr. Polym.* **2019**, *212*, 222−228.
(26) Chiu, Y. C.; Otsuka, I.; Halila, S.; Borsali, R.; Chen, W. C. High-Performance Nonvolatile Transistor Memories of Pentacence Using the Green Electrets of Sugar-based Block Copolymers and Their Supramolecules. *Adv. Funct. Mater.* **2014**, *24*, 4240−4249.
(27) Chiu, Y. C.; Sun, H. S.; Lee, W. Y.; Halila, S.; Borsali, R.; Chen, W. C. Oligosaccharide Carbohydrate Dielectrics toward High Performance Non-volatile Transistor Memory Devices. *Adv. Mater.* **2015**, *27*, 6257−6264.
(28) Bosworth, J. K.; Paik, M. Y.; Ruiz, R.; Schwartz, E. L.; Huang, J. Q.; Ko, A. W.; Smilgies, D. M.; Black, C. T.; Ober, C. K. Control of Self-Assembly of Lithographically Patternable Block Copolymer Films. *ACS Nano* **2008**, *2*, 1396−1402.
(29) Paik, M. Y.; Bosworth, J. K.; Smilges, D. M.; Schwartz, E. L.; Andre, X.; Ober, C. K. Reversible Morphology Control in Block Copolymer Films via Solvent Vapor Processing: An in Situ GISAXS Study. *Macromolecules* **2010**, *43*, 4253−4260.
(30) Mokarian-Tabari, P.; Collins, T. W.; Holmes, J. D.; Morris, M. A. Cyclical "Flipping" of Morphology in Block Copolymer Thin Films. *ACS Nano* **2011**, *5*, 4617−4623.
(31) Seppala, J. E.; Lewis, R. L.; Epps, T. H. Spatial and Orientation Control of Cylindrical Nanostructures in ABA Triblock Copolymer Thin Films by Raster Solvent Vapor Annealing. *ACS Nano* **2012**, *6*, 9855−9862.
(32) Sinturel, C.; Vayer, M.; Morris, M.; Hillmyer, M. A. Solvent Vapor Annealing of Block Polymer Thin Films. *Macromolecules* **2013**, *46*, 5399−5415.
(33) Kim, S.; Li, W.; Fredrickson, G. H.; Craig, J. H.; Kramer, E. J. Order−Disorder Transition in Thin Films of Horizontally-Oriented Cylinder-Forming Block Copolymers: Thermal Fluctuations vs. Preferential Wetting. *Soft Matter* **2016**, *12*, 5915.
(34) Choi, Y. J.; Byun, M. H.; Park, T. W.; Choi, S.; Bang, J.; Jung, H.; Cho, J. H.; Kwon, S. H.; Kim, K. H.; Parl, W. I. Rapid and Cyclable Morphology Transition of High-χ Block Copolymers via Solvent Vapor-Immersion Annealing for Nanoscale Lithography. *ACS Appl. Nano Mater.* **2019**, *2*, 1294−1301.
(35) Xiao, Z.; Dong, Q.; Bi, C.; Shao, Y.; Yuan, Y.; Huang, J. Solvent Annealing of Perovskite-Induced Crystal Growth for Photovoltaic-Device Efficiency Enhancement. *Adv. Mater.* **2014**, *26*, 6503−6509.
(36) Lan, S.; Yang, H.; Zhang, G.; Wu, X.; Chen, Q.; Chen, L.; Chen, H.; Guo, T. Importance of Solvent Removal Rate on the Morphology and Device Performance of Organic Photovoltaics with Solvent Annealing. *ACS Appl. Mater. Interfaces* **2017**, *9*, 20679−20685.
(37) Datt, R.; Bagui, A.; Siddiqui, A.; Sharma, R.; Gupta, V.; Yoo, S.; Kumar, S.; Singh, S. P. Effectiveness of Solvent Vapor Annealing over Thermal Annealing on the Photovoltaic Performance of Non-Fullerene Acceptor Based BHJ Solar Cells. *Sci. Rep.* **2019**, *9*, No. 8529.
(38) Wienhold, K. S.; Körstgens, V.; Grott, S.; Jiang, X.; Schwartzkopf, M.; Roth, S. V.; Müller-Buschbaum, P. Effect of Solvent Additives on the Morphology and Device Performance of Printed Nonfullerene Acceptor Based Organic Solar Cells. *ACS Appl. Mater. Interfaces* **2019**, *11*, 42313−42321.
(39) Khim, D.; Baeg, K.-J.; Kim, J.; Kang, M.; Lee, S.-H.; Chen, Z.; Facchetti, A.; Kim, D.-Y.; Noh, Y.-Y. High Performance and Stable N-channel Organic Field-effect Transistors by Patterned Solvent-Vapor Annealing. *ACS Appl. Mater. Interfaces* **2013**, *5*, 10745−10752.
(40) Jeon, G. G.; Lee, M.; Nam, J.; Park, W.; Yang, M.; Choi, J.-H.; Yoon, D. K.; Lee, E.; Kim, B.; Kim, J. H. Simple Solvent Engineering for High-Mobility and Thermally Robust Conjugated Polymer Nanowire Field-Effect Transistors. *ACS Appl. Mater. Interfaces* **2018**, *10*, 29824−29830.

https://dx.doi.org/10.1021/acsami.0c04551
ACS Appl. Mater. Interfaces 2020, 12, 23217−23224